


## PAPER



Cite this: *Nanoscale Adv.*, 2023, 5, 2646

# Single-phase BiFeO<sub>3</sub> and BiFeO<sub>3</sub>–Fe<sub>2</sub>O<sub>3</sub> nanocomposite photocatalysts for photodegradation of organic dye pollutants†

Pravallika Banoth,<sup>a</sup> Boya Palajonnala Narsaiah,<sup>b</sup> Luis De Los Santos Valladares,<sup>\*cd</sup> Jumat Kargin<sup>e</sup> and Pratap Kollu <sup>\*ab</sup>

The application of a novel BiFeO<sub>3</sub> (BFO)–Fe<sub>2</sub>O<sub>3</sub> composite (called BFOF) as a photocatalyst for the degradation of methylene blue is reported. To improve the photocatalytic effectiveness of BiFeO<sub>3</sub>, we synthesized the first BFOF photocatalyst by adjusting the molar ratio of Fe<sub>2</sub>O<sub>3</sub> in BiFeO<sub>3</sub> using microwave-assisted co-precipitation. The UV-visible properties of the nanocomposites showed excellent absorption of visible light and reduced electron–hole recombination properties compared to the pure phase BFO. Photocatalytic studies on BFOF10 (90% BFO, 10% Fe<sub>2</sub>O<sub>3</sub>), BFOF20 (80% BFO, 20% Fe<sub>2</sub>O<sub>3</sub>), and BFOF30 (70% BFO, 30% Fe<sub>2</sub>O<sub>3</sub>) have shown that they decompose Methylene Blue (MB) in sunlight better than the pure BFO phase in 70 minutes. The BFOF30 photocatalyst was the most effective at reducing MB when exposed to visible light (94%). Magnetic studies confirm that the most effective catalyst BFOF30 has excellent stability and magnetic recovery properties due to the presence of magnetic phase Fe<sub>2</sub>O<sub>3</sub> in the BFO.

Received 2nd December 2022  
Accepted 22nd March 2023

DOI: 10.1039/d2na00881e

rsc.li/nanoscale-advances

## 1. Introduction

Due to the difficulty in recovering photocatalysts from the majority of treated solutions and reusing them, it is challenging to bring composite photocatalysis to the practical application because it is difficult to recover them from treated solutions. Nano and microparticles with a large surface area possess high photocatalytic activity,<sup>1,2</sup> allowing better spreading in aqueous media.<sup>3</sup> They efficiently pass the light needed for the catalysts to be photoactivated. However, recovering those tiny particles through filtration or centrifugation typically results in higher operating costs for photocatalyst reuse in subsequent cycles. During the past decade, researchers have used external magnetic fields to separate magnetized photocatalytic materials from aqueous phases. Various pure and composite materials have been widely studied, including single-phase ferromagnetic

BiFeO<sub>3</sub>, Fe<sub>3</sub>O<sub>4</sub>/TiO<sub>2</sub>, Fe<sub>2</sub>O<sub>3</sub>/ZnO, BiFeO<sub>3</sub>/SrTiO<sub>3</sub>, Fe<sub>2</sub>O<sub>3</sub>/TiO<sub>2</sub>, and BiFeO<sub>3</sub>/Fe<sub>2</sub>O<sub>3</sub>.<sup>4–10</sup>

Most of the above-mentioned magnetic materials have shown excellent photocatalytic activity and performance for degrading organic pollutants and other dyes, as well as practical ways to quickly recover powder (catalyst) from the suspension.<sup>4–10</sup> Among the oxide semiconductors, BiFeO<sub>3</sub> and Fe<sub>2</sub>O<sub>3</sub> have attracted particular attention because of their chemical stability, magnetic properties and excellent optical properties in visible light, which could make a significant difference in the absorption of visible light by solar energy over other semiconductors such as GaS, CdS and ZnS.<sup>11,12</sup> Although numerous studies have demonstrated a bit of improvement in the photocatalytic activity of BFO and Fe<sub>2</sub>O<sub>3</sub>, still the photocatalytic performance of the pure phase BFO and pure phase Fe<sub>2</sub>O<sub>3</sub> is lower than those of other oxide semiconductor visible light-active photocatalysts, such as BiVO<sub>4</sub>,<sup>13,14</sup> BiOX (X = Cl, I, Br)<sup>15–17</sup> or Bi<sub>2</sub>O<sub>3</sub> (ref. 18–20) due to their wide energy bandgap, improper optical band positions and high rates of electron and hole recombination compared to other commercially available semiconductors mentioned above.<sup>21–23</sup>

Combining multiple photocatalysts and creating a composite photocatalyst system are among the advantageous techniques for promoting photogenerated electron–hole pairs and their separation.<sup>24–26</sup> Recently, researchers have developed several composites of visible photocatalysts such as CuO/BFO,<sup>27</sup> BFO/polymer g-C<sub>3</sub>N<sub>4</sub>, g-C<sub>3</sub>N<sub>4</sub>/BFO,<sup>28</sup> BaTiO<sub>3</sub>/α-Fe<sub>2</sub>O<sub>3</sub> (ref. 29) and core–shell structures Fe<sub>2</sub>O<sub>3</sub>@CeO<sub>2</sub> (ref. 30) showing improved photocatalytic activity. Like the BiFeO<sub>3</sub> system,<sup>31</sup> α-

<sup>a</sup>School of Physics, University of Hyderabad, Prof. C. R. Rao Road, Gachibowli, Hyderabad 500046, Telangana, India. E-mail: pratapk@uohyd.ac.in

<sup>b</sup>CASEST, School of Physics, University of Hyderabad, Prof. C. R. Rao Road, Gachibowli, Hyderabad 500046, Telangana, India

<sup>c</sup>Cavendish Laboratory, Department of Physics, University of Cambridge, J. J. Thomson Avenue, Cambridge CB3 0HE 2, UK

<sup>d</sup>Laboratorio de Cerámicos y Nanomateriales, Facultad de Ciencias Físicas, Universidad Nacional Mayor de San Marcos, Ap. Postal 14-0149, Lima, Peru

<sup>e</sup>Faculty of Physics and Technology, L. N. Gumilyov Eurasian National University, 010000 Nur Sultan, Kazakhstan

† Electronic supplementary information (ESI) available. See DOI: <https://doi.org/10.1039/d2na00881e>



$\text{Fe}_2\text{O}_3$  (hematite) possesses a canted antiferromagnetic alignment and a rhombohedral crystal structure.<sup>32</sup> Both crystal systems exhibit small optical band gaps ( $E_{\text{g}(\text{BiFeO}_3)} = 2.2\text{--}2.8$  eV (ref. 33 and 34) and  $E_{\text{g}(\alpha\text{-Fe}_2\text{O}_3)} = 2.2$  eV), making them suitable for photocatalysis and photoelectrochemical applications.<sup>35</sup> In addition, the particle's size, strain, and defect impact its magnetic and optical properties.<sup>36</sup> It has been reported that  $\gamma$ - and  $\alpha\text{-Fe}_2\text{O}_3$  in  $\text{BiFeO}_3$  increase strain and magnetization, with the feasibility of  $\alpha\text{-Fe}_2\text{O}_3$  to be easily incorporated into a  $\text{BiFeO}_3$  matrix.<sup>37</sup> Therefore,  $\text{BiFeO}_3/\alpha\text{-Fe}_2\text{O}_3$  composites are interesting to study in terms of their structural and physical properties.<sup>38</sup>

In the present work, we have synthesized the BFO-based composites  $\text{BiFeO}_3\text{-Fe}_2\text{O}_3$  by loading different ratios of hollow micro spherical  $\text{Fe}_2\text{O}_3$  (10, 20 and 30%) into the BFO micro flowers. Very few studies have been done on the  $\text{BiFeO}_3/\text{Fe}_2\text{O}_3$  composites.<sup>39–42</sup> A novel aspect of the current study is that the  $\alpha\text{-Fe}_2\text{O}_3$  hollow spheres have been collected from the slags generated by the steel industry. Moreover, the microwave-assisted co-precipitation method was used to construct  $\text{BFO-Fe}_2\text{O}_3$  composites by mixing different molar ratios of BFO and  $\text{Fe}_2\text{O}_3$  hollow microspheres. Despite irradiation for 70 min under sunlight illumination, the  $\text{BFO-Fe}_2\text{O}_3$  composite (also known as BFOF in the rest of the paper) has shown outstanding photocatalytic activity for eliminating methylene blue. After adding different ratios of  $\text{Fe}_2\text{O}_3$  into the BFO, the BFOF composites have shown enhanced magnetic properties, photocatalytic activity and magnetic recovery compared to the pure phase BFO.

## 2. Experimental section

### 2.1. Materials used for the preparation of $\text{BiFeO}_3\text{-Fe}_2\text{O}_3$ composites

For this procedure, ethanol, double-distilled water (DDW), pure potassium hydroxide (KOH, SRL, 98%), pure ferric chloride ( $\text{FeCl}_3 \cdot 6\text{H}_2\text{O}$ , SRL, 98%), ferric nitrate nonahydrate [ $\text{Fe}(\text{NO}_3)_3 \cdot 9\text{H}_2\text{O}$ , SRL, 98%], mono-hydrated citric acid ( $\text{C}_6\text{H}_8\text{O}_7 \cdot \text{H}_2\text{O}$ , Sigma, 99.99%), and pure bismuth chloride ( $\text{BiCl}_3$ , SRL, 98%) are all used.

### 2.2. Preparation of $\text{BiFeO}_3$ micro flowers

The pure phase BFO is synthesized by the microwave-assisted-solvothermal (MWAST) method in a domestic solo-microwave oven with power 800 W and operating at 2.45 GHz. We have prepared the BFO in powder form with two metal precursors ( $\text{BiCl}_3$ ,  $\text{FeCl}_3 \cdot 6\text{H}_2\text{O}$ ) and a mineralizer (KOH). A solution of equimolar concentrations (0.05 M) of  $\text{BiCl}_3$  and  $\text{FeCl}_3 \cdot 6\text{H}_2\text{O}$  was dissolved in ethanol and mechanically stirred for 1 hour. The dropwise addition of 8 M KOH solution altered the original solution. A hydroxide precipitate of bismuth and iron was obtained after 30 minutes of magnetic stirring. Later, 10 ml of this mixture was poured into a customized sealed microwave acid digestion vessel (model 4782 from Parr) of 45 ml capacity and then placed in a homemade microwave oven. The chemical reactions were carried out by applying a microwave power level of 800 W at a constant microwave heating time of 3 minutes and allowing the reaction vessel to cool down to room temperature.

The final reaction residue was washed in DDW several times and dried at 80 °C for 4 hours.<sup>43</sup>

### 2.3. Preparation of hollow $\text{Fe}_2\text{O}_3$ microspheres

The hematite sample was collected from slag generated during the hot rolling process from the steel industry in Kazakhstan. It is obtained as a secondary product during steel production described elsewhere which can produce iron oxide particles.<sup>44,45,53</sup> The collected samples were used as such without treatment with any harmful compounds. In previous studies we have characterized these steel slags, see ref. 44 and 45. They consist of stable polycrystalline  $\alpha\text{-Fe}_2\text{O}_3$  hollow spheres with diameters around 1  $\mu\text{m}$ . More detailed information about the formation of the hematite during steel production is described in the ESI.†

### 2.4. Synthesis of $\text{BFO-Fe}_2\text{O}_3$ composites

$\text{BFO-Fe}_2\text{O}_3$  composites are prepared by a simple coprecipitation method following microwave heating at 360 W for 3 min. We dissolved a stoichiometric ratio of BFO and  $\text{Fe}_2\text{O}_3$  powders in 40 ml of ethanol and sonicated it for six hours at 80 °C to evaporate the solvent and obtain the gel. Finally, the gel was heated at 360 W for 3 min in a domestic microwave oven. Following the above procedure, we have synthesized three different series of  $\text{BFO-Fe}_2\text{O}_3$  composites by loading different ratios of  $\text{Fe}_2\text{O}_3$  into the BFO. The prepared composites  $\text{BFO-Fe}_2\text{O}_3$  (10, 20 and 30%) are named BFOF10, BFOF20, and BFOF30, respectively.

## 3. Characterization

The synthesized BFO,  $\text{Fe}_2\text{O}_3$  and composites were characterized using UV-visible spectroscopy (Jasco V-670 UV-visible double beam spectrophotometer) against deionized water as blank. The absorption spectra were recorded in the 200–800 nm wavelength range. By analysing XRD data (PANalytical, X'Pert Powder Diffractometer), we have confirmed the formation of the pure phases of BFO,  $\text{Fe}_2\text{O}_3$  and composites. In this diffractogram, the scanning range was between 20° and 80° ( $2\theta$  value) at a scan rate of 4°  $\text{min}^{-1}$ , and the step size was 0.02°. Field emission scanning electron microscopy (FESEM: Carl Zeiss Smart Sem) and energy dispersive X-ray analysis (EDAX) were used to study the morphology of the synthesized samples. A vibrating sample magnetometer (VSM) measured the magnetic properties of synthesized samples at room temperature (VSM, Model: LakeShore).

## 4. Photocatalysis

Using a model pollutant dye Methylene Blue (MB), each prepared sample was assessed for its photocatalytic activity for degrading dye pollutants. Photodegradation was conducted in heavy sunlight (200  $\text{mW cm}^{-2}$ ). A total of 40 mg of each photocatalyst powder was initially added to 100 ml of MB solution at a concentration of 10  $\text{mg L}^{-1}$  and neutral pH. Following continuous magnetic stirring, the slurry was irradiated with heavy sunlight. We monitored the decolourization of the dye

solution using UV-visible spectroscopy in the range of 200 to 800 nm.

## 5. Results and discussion

### 5.1. X-ray diffraction (XRD) analysis of the composites

We synthesized BFO-Fe<sub>2</sub>O<sub>3</sub> composite powders, along with content levels (mass%) of Fe<sub>2</sub>O<sub>3</sub> of 10% (BFOF10), 20% (BFOF20) and 30% (BFOF30) using the chemical coprecipitation method. The XRD patterns of the BFO, Fe<sub>2</sub>O<sub>3</sub> and BFO-Fe<sub>2</sub>O<sub>3</sub> composites are displayed in Fig. 1.

According to XRD analysis, the BFO exhibited Rhombohedral crystal structures with the *R3c* space group, which is in perfect agreement with the previous crystallographic data (ICSD 98-019-1940), exhibiting no secondary phases within the detection limits of the technique. It was determined that the Fe<sub>2</sub>O<sub>3</sub> XRD pattern showed Rhombohedral symmetry (*R3c* space group, ICSD: 98-005-6372). After adding 10% of Fe<sub>2</sub>O<sub>3</sub> (BFOF10), the XRD patterns showed all peaks corresponding to pure phase BFO with a slight trace of the two prominent peaks (104) and (110) of Fe<sub>2</sub>O<sub>3</sub>. As the Fe<sub>2</sub>O<sub>3</sub> loading ratio increased to 20% (BFOF20), more Fe<sub>2</sub>O<sub>3</sub> peaks appeared. In particular, the increased intensity of the two most intense Fe<sub>2</sub>O<sub>3</sub> peaks found at about 33.38 and 35.83°, corresponding to (104) and (110) crystal orientations, confirms the higher Fe<sub>2</sub>O<sub>3</sub> content. Finally, after loading 30% Fe<sub>2</sub>O<sub>3</sub>, the composite sample BFOF30 presents all the Fe<sub>2</sub>O<sub>3</sub> peaks besides the diffraction pattern corresponding to pure BFO.

### 5.2. FE-SEM images of BFO-Fe<sub>2</sub>O<sub>3</sub> composites

As shown in Fig. 2, FE-SEM was used to analyse the microstructures of the BFO-Fe<sub>2</sub>O<sub>3</sub> composites. Fig. 2(a) shows that pure phase BFO powder was composed of many BFO micro flowers where hundreds of BFO nano petals were closely packed on the BFO micro flowers.<sup>46</sup> Microstructures of pure phase

Fe<sub>2</sub>O<sub>3</sub> are shown in Fig. 2(b), confirming the formation of hollow Fe<sub>2</sub>O<sub>3</sub> microspheres. As illustrated in Fig. 2(c)–(e), the microstructure of the BFO-Fe<sub>2</sub>O<sub>3</sub> composite is drastically altered after different molar ratios of Fe<sub>2</sub>O<sub>3</sub> hollow microspheres were loaded on BFO. It is worth mentioning that after heating the BFO-Fe<sub>2</sub>O<sub>3</sub> composites with high microwave energy (350 W, 3 min), both BFO micro flowers and hollow Fe<sub>2</sub>O<sub>3</sub> microspheres were destroyed. From Fig. 2(c), it can be seen that there is partial contact between the BFO and Fe<sub>2</sub>O<sub>3</sub> phases. It is believed that the destroyed nano petals from BFO micro flowers enter into the hollow Fe<sub>2</sub>O<sub>3</sub> microspheres and make the coupling between the BFO and Fe<sub>2</sub>O<sub>3</sub> phases, which is a crucial factor for enhancing the photocatalytic activity. As the amount of Fe<sub>2</sub>O<sub>3</sub> increases, the contact between both phases increases, as shown in Fig. 2(d) and (e). The EDAX spectra of BFOF10, BFOF20, and BFOF30 are shown in Fig. 2(f)–(h). It is proven that the Bi, Fe, and O components are the source of the signal peaks, indicating that Fe<sub>2</sub>O<sub>3</sub> was successfully loaded into the BFO.

### 5.3. TEM images of the BFO-Fe<sub>2</sub>O<sub>3</sub> composite

Fig. 3(a)–(c) show the TEM images of the BFO-Fe<sub>2</sub>O<sub>3</sub> composite. This figure shows that the composite material was composed of BFO nanoflowers with thin nanocrystalline petals of size 50 nm on the surface and Fe<sub>2</sub>O<sub>3</sub> spheres. One can clearly see the contact between the two phases in the composite. To further investigate the detailed structural information of contact between both phases in the BFO-Fe<sub>2</sub>O<sub>3</sub> composite, high-resolution transmission electron microscopy (HRTEM) was performed. In the HRTEM image (Fig. 3(d)), the BFO nano petals collected from the BFO-Fe<sub>2</sub>O<sub>3</sub> composite revealed well-resolved lattice fringes with an interplanar distance of 0.281, 0.396 and 0.239 nm corresponding to the (104), (012) and (113) planes of the BFO rhombohedral structure respectively in all the composite materials [Fig. 3(d) and (e)]. The Fe<sub>2</sub>O<sub>3</sub> hollow spheres with small size showed lattice fringes with 0.251 and 0.367, and 0.269 nm interplanar distances corresponding to the (110), (012) and (104) planes of the Fe<sub>2</sub>O<sub>3</sub> hexagonal structure, respectively [Fig. 3(d) and (e)]. As a result, the TEM analysis also confirms the phases of BFO and Fe<sub>2</sub>O<sub>3</sub> in the BFO-Fe<sub>2</sub>O<sub>3</sub> composite, which is consistent with the FESEM and EDAX analysis.

### 5.4. Optical properties of BFO-Fe<sub>2</sub>O<sub>3</sub> composites

The UV-vis absorption spectrum of all the prepared samples is shown in Fig. 4. Each sample demonstrated an excellent visible light absorption that matches extremely well with the majority of the UV-vis spectra of single-phase Fe<sub>2</sub>O<sub>3</sub> and their composites that have been published.<sup>47,48</sup> BFOF10, BFOF20, and BFOF30 exhibit excellent optical absorption in the visible range, demonstrating their suitability for visible photodegradation of organic dyes. The shoulder peaks observed besides the prominent peak in all the samples correspond to the metal-to-metal transitions. The absorption of light in the visible spectral range from 500–800 nm increased as the amount of Fe<sub>2</sub>O<sub>3</sub> increased, revealing that the visible light absorbance of these composites improved more than the pure phase BFO. The improvement in

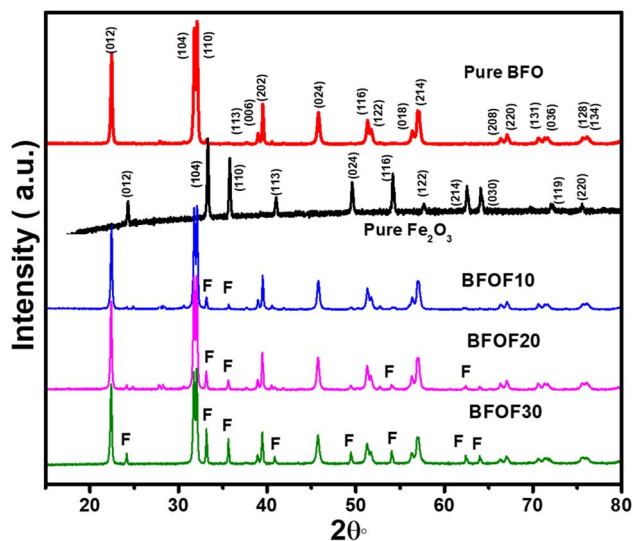


Fig. 1 XRD patterns of pure BFO, pure Fe<sub>2</sub>O<sub>3</sub>, BFOF10, BFOF20, and BFOF30.

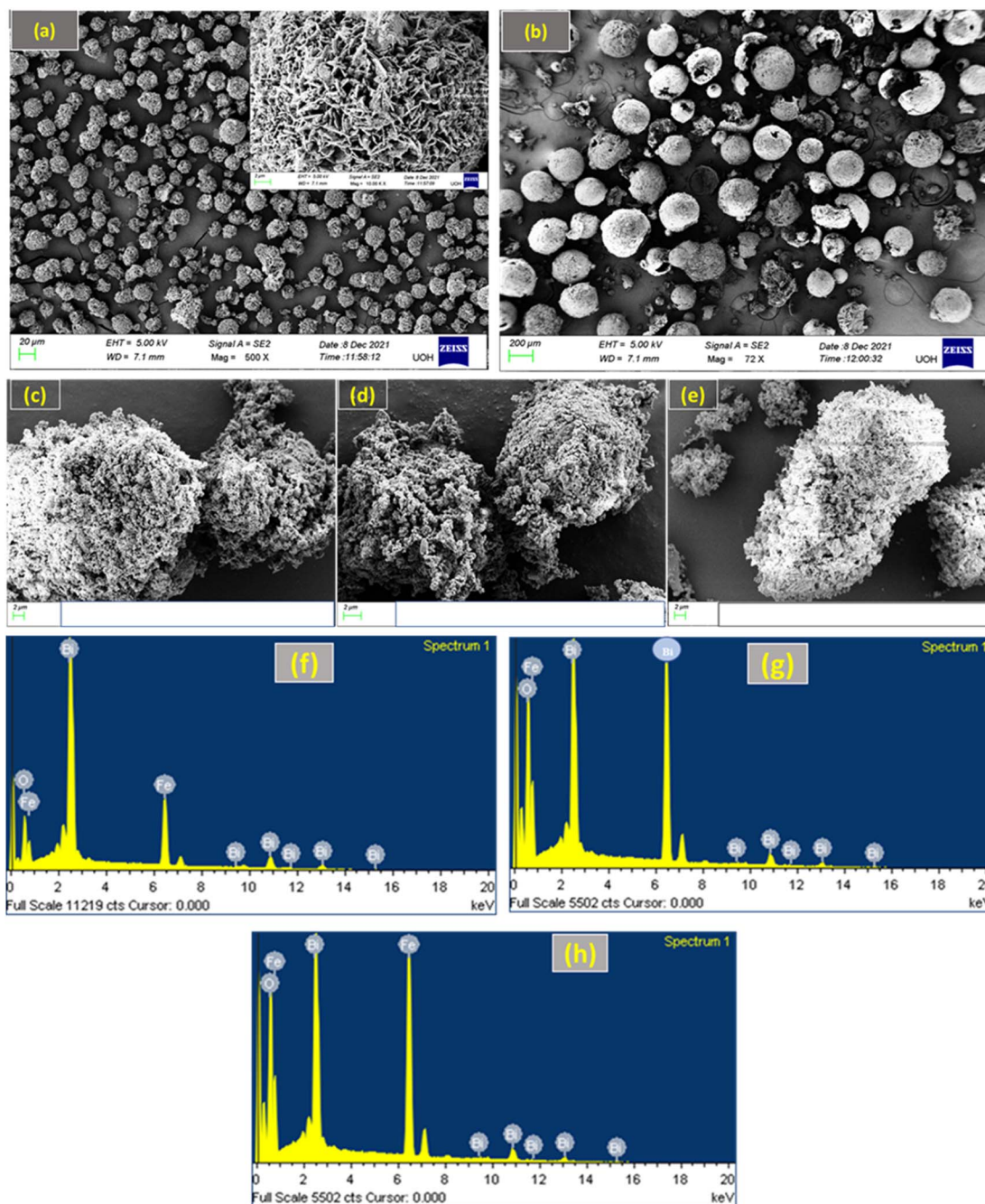


Fig. 2 FE-SEM images of (a) pure BFO, (b) pure Fe<sub>2</sub>O<sub>3</sub>, (c) BFOF10, (d) BFOF20, and (e) BFOF30, and EDAX spectra of (f) BFOF10, (g) BFOF20, and (h) BFOF30.

light absorption is most probably due to the enhancement in the production of photo-excited electrons and holes. When we combine two different semiconducting materials, there will be heterojunction formation at the interface due to the coupling of the two different energy band gaps. Due to the Schottky effect, there will be inhibition of the transformation of hole–electron pairs from one semiconductor to another, which results in a reduction in the hole–electron recombination rate; thus, there is an enhancement in the light absorption property of the material. Every material from the BFO–Fe<sub>2</sub>O<sub>3</sub> composite will provide a high number of photoexcited electrons and holes and

produce a high number of oxidation and reduction reactions, resulting in reactive species production. This results in an increment in the photocatalytic activity of any material. The obtained band energies of these composites, BFOF10 (570 nm), BFOF20 (579 nm), and BFOF30 (620 nm), were 2.17, 2.14, and 2.0 eV [Table 1]. According to the results of the bandgap studies, the energy band gap of these composites is smaller than that of the pure phase BFO, which might be because two semiconductors' interfaces combine two different energy band gaps. This study observed that BFOF30 has a higher absorption of light in the visible range with a lower bandgap than the other

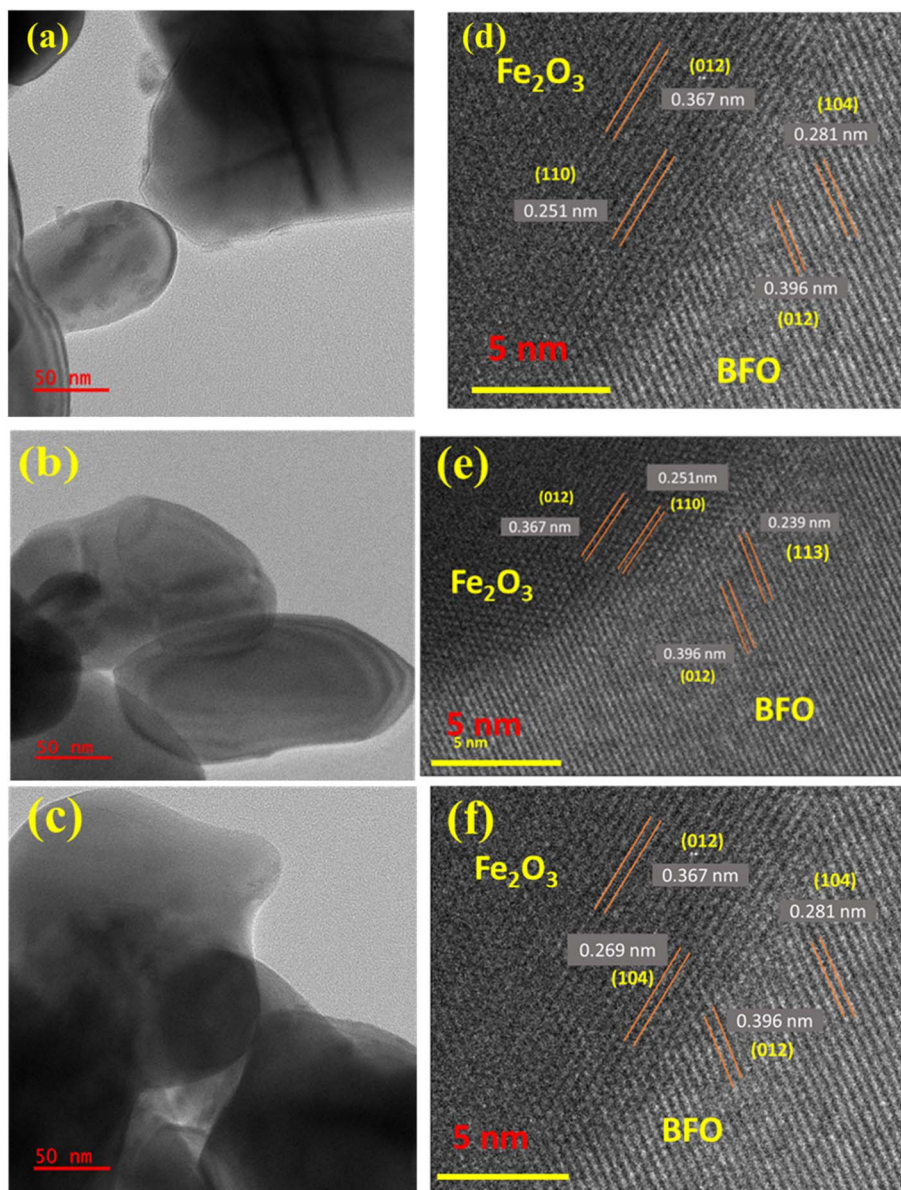


Fig. 3 TEM images of (a) BFOF10, (b) BFOF20, and (c) BFOF30 and HRTEM images of (d) BFOF10, (e) BFOF20 and (f) BFOF30.

two (BFOF10 and BFOF20) and is expected to produce a higher number of photogenerated electron holes. Using Tauc's plot, we calculated the optical band edges as follows:

$$(\alpha h\nu) = A(h\nu - E_g)^n$$

$\alpha$  is the absorption coefficient,  $E_g$  represents the energy band gap,  $A$  is constant, and depending on transition, we have to consider  $n$  values.

- Directly permitted transitions,  $n = 1/2$ .
- Directly forbidden transitions,  $n = 3/2$ .
- Permitted indirect transitions,  $n = 2$ .
- Indirect prohibited transitions,  $n = 3$ .

### 5.5. Photocatalytic activity of BFO-Fe<sub>2</sub>O<sub>3</sub> composites

Fig. 5 displays the photocatalytic capabilities of BFO, Fe<sub>2</sub>O<sub>3</sub>, and BFO-Fe<sub>2</sub>O<sub>3</sub> composites under heavy sunlight. The complete degradation of MB using the BFO, Fe<sub>2</sub>O<sub>3</sub> and BFO-Fe<sub>2</sub>O<sub>3</sub> composite took 70 minutes to complete. The equation for calculating the performance of the photocatalyst is given below.  $C_0$  is an initial concentration of MB, and  $C_t$  is the concentration at time  $t$ .

$$\text{Efficiency} = \frac{C_0 - C_t}{C_0} \times 100$$

After adding 10% Fe<sub>2</sub>O<sub>3</sub> [BFOF10], we observed less degradation (72%) in the MB solution compared to the other two composites [BFOF20, BFOF30]. The photocatalytic efficiency of

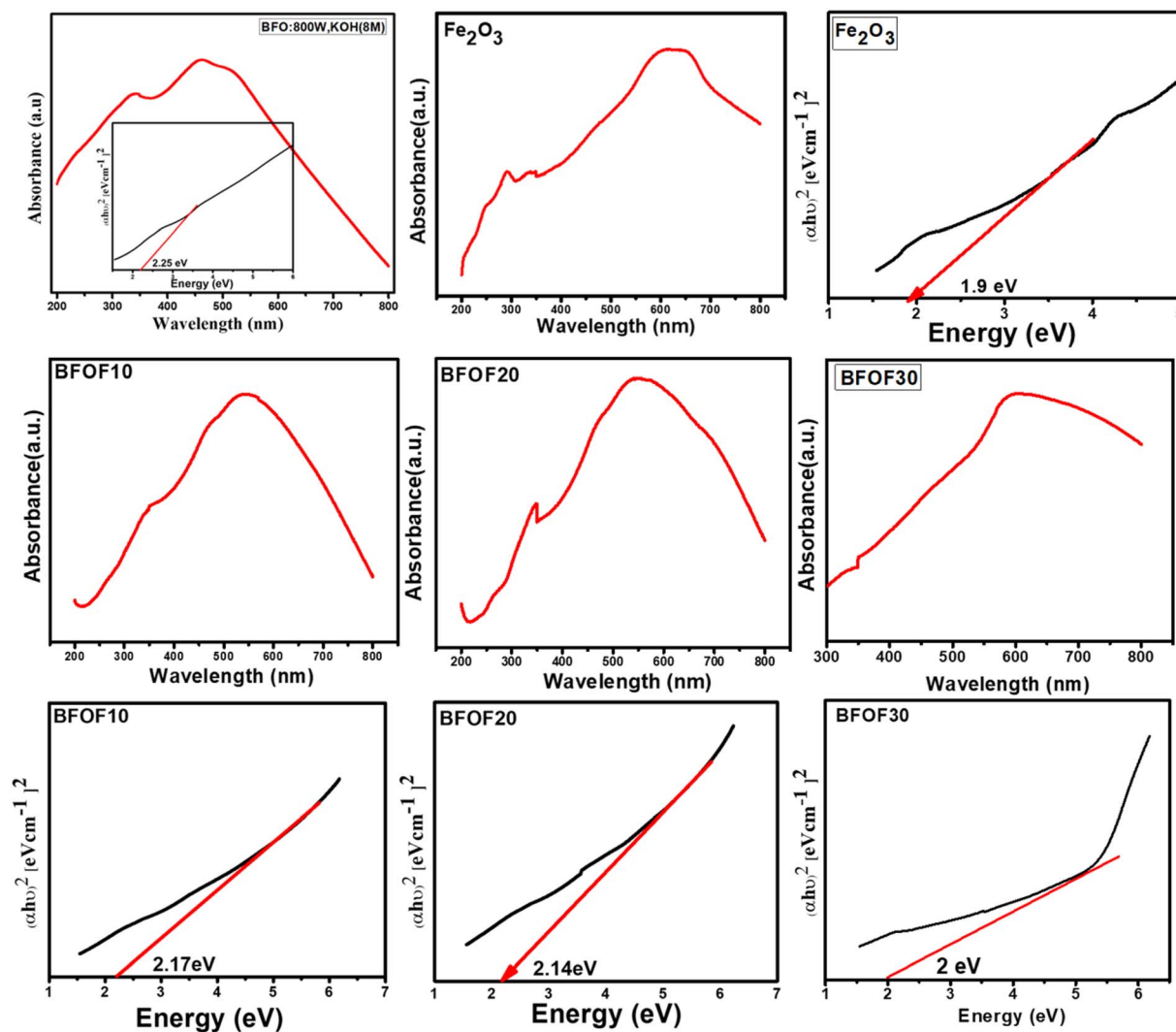


Fig. 4 UV-vis absorption spectra and energy band gaps of  $\text{Fe}_2\text{O}_3$ , BFOF10, BFOF20, and BFOF30.

Table 1 Band energies obtained from optical property studies

S. no	Sample	The band gap (eV)
1	BFO	2.25
2	$\text{Fe}_2\text{O}_3$	1.9
3	BFOF10	2.17
4	BFOF20	2.14
5	BFOF30	2.0

BFOF20 and BFOF30 has increased to 86, and 94%, respectively. The increased photocatalytic performance of the samples BFOF20 and BFOF30 demonstrates how efficiency increased for higher concentrations of  $\text{Fe}_2\text{O}_3$ . The composite's microstructural characteristics may cause this improvement in photodegradation efficiency. The BFO surface is entirely coupled with  $\text{Fe}_2\text{O}_3$  in this situation (BFOF20 and BFOF30), making it easier for the light to form electron-hole pairs at the BFO- $\text{Fe}_2\text{O}_3$

surface, and also the band gaps of BFOF20 and BFOF30 are narrower than that of the pure BFO sample. As a result, their photocatalytic efficiency is improved. In this photodegradation test, the composites demonstrated significantly higher photodegradation efficiency than pure phase BFO, demonstrating the ability of these composites to degrade MB in sunlight.

### 5.6. Effect of photocatalyst concentration on efficiency

The degradation of MB dye was carried out at a constant dosage of  $10 \text{ mg L}^{-1}$  using different composites of BFOF10, BFOF20, and BFOF30 at different catalyst dosages (10, 20, 30 and 40 mg). The catalyst dosage, the initial dosage of dye, the type of dye, the pH value of the dye, and most microstructures of the catalysts were all factors that affected the dye degradation.<sup>49</sup> Fig. 6 demonstrates that the catalyst concentration significantly impacts the photodegradation efficiency by showing that the photodegradation efficiency of MB decreases as the catalyst concentration increases (all values obtained are presented in Table 2). According to the literature, microstructure, pH level,

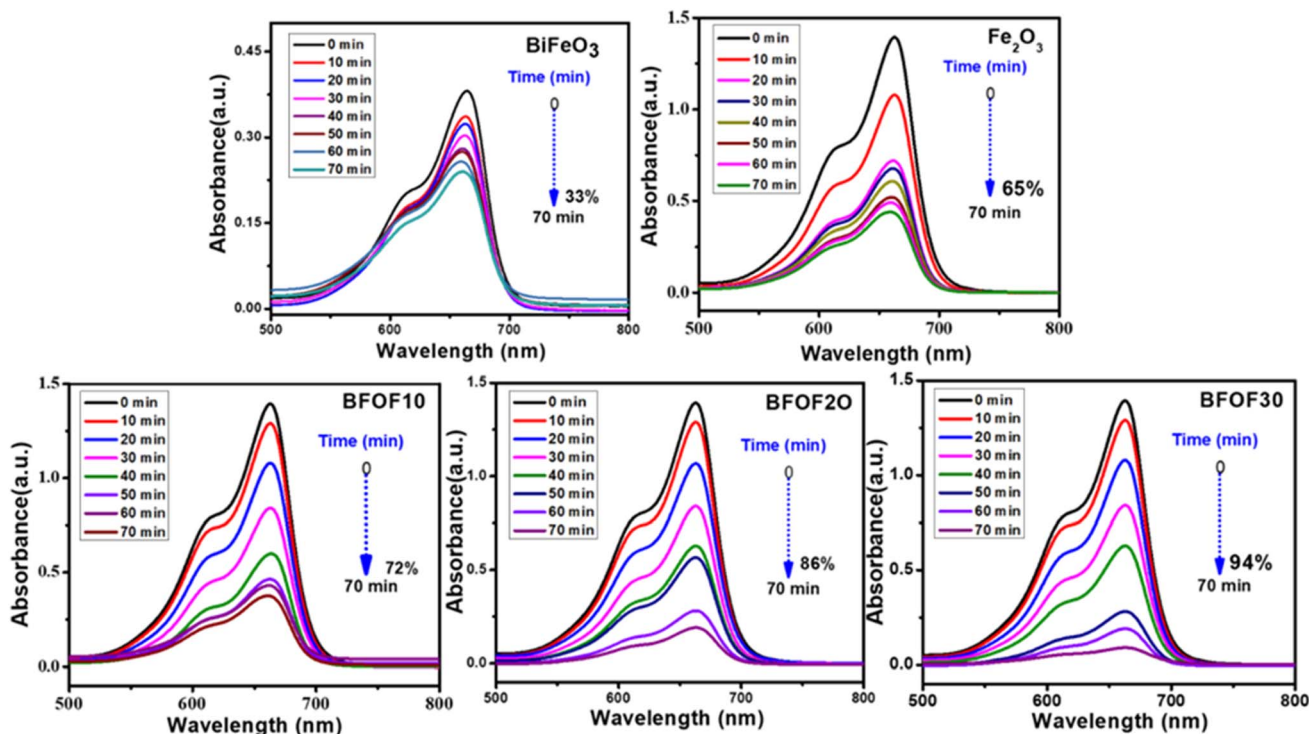


Fig. 5 Time dependent UV-vis spectral changes of methylene blue in the presence of BFO,  $\text{Fe}_2\text{O}_3$ , BFOF10, BFOF20, and BFOF30.

dye concentration, and other factors significantly impact photodegradation efficiency.<sup>49–52</sup>

### 5.7. Stability and magnetic recovery of photocatalysts

The catalyst stability of the most active powders, BFOF20 and BFOF30, was investigated by recycling them for four cycles. Fig. 7 shows no difference in the photodegradation efficiencies of the BFOF20 and BFOF30 catalysts for the first two cycles. Only a 6% and 4% decline in the efficiency of BFOF20 and BFOF30, respectively, is visible after four cycles, demonstrating the stability of the suggested catalysts for the first four cycles.

The magnetization curves for the composites and the pure phase BFO and  $\text{Fe}_2\text{O}_3$  are shown in Fig. 8(a) and (b). Compared to BFO ( $1.25 \text{ emu g}^{-1}$ ), the magnetization value of BFO– $\text{Fe}_2\text{O}_3$  composites increases with increasing  $\text{Fe}_2\text{O}_3$  content ( $1.84 \text{ emu}$

Table 2 Influence of catalyst dosage (mg) on photodegradation (%)

Catalyst name	Catalyst dosage (mg)	Degradation (%)
BFOF10	10	54
	20	62
	30	68
	40	72
BFOF20	10	58
	20	62
	30	75
	40	86
BFOF30	10	71
	20	76
	30	89
	40	94

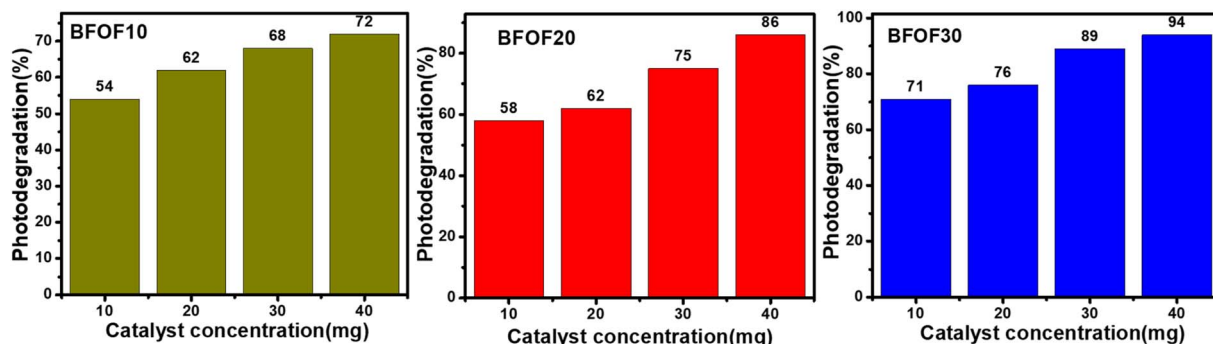


Fig. 6 Effect of photocatalyst dosage on the photodegradation efficiency of composites BFOF10, BFOF20, and BFOF30.

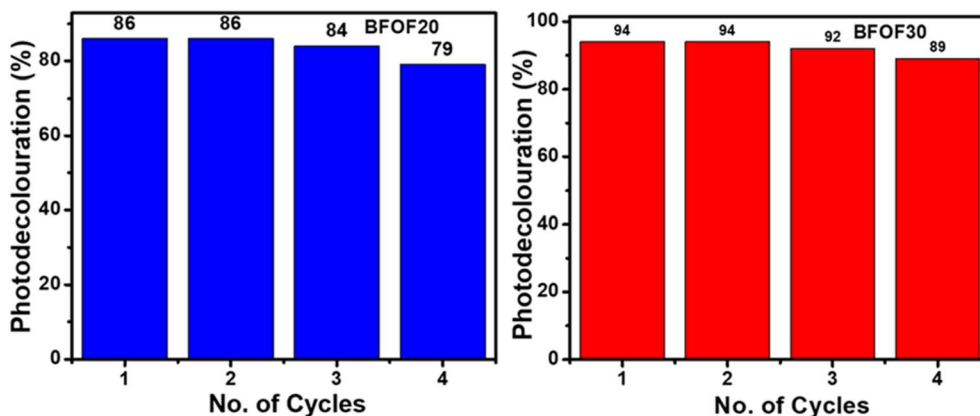


Fig. 7 Photodegradation efficiency of composites BFOF20 and BFOF30 after four cycles.

$g^{-1}$ ). The most efficient sample, BFOF30, had a maximum magnetism of  $1.58 \text{ emu } g^{-1}$ , which is adequate for magnetic recovery. Fig. 8(c) displays the magnetization values for the prepared samples. The improvement in the magnetization value of BFOF composites is due to the presence of magnetic phase  $Fe_2O_3$  in the BFO phase.

We have tested the magnetic recovery property of BFOF30 since it is the most efficient catalyst among the three BFO- $Fe_2O_3$  composites. As shown in Fig. 9, using a magnetic field enables us to recover the BFOF30 catalyst quickly since it has an excellent magnetic response to the applied magnetic field. A permanent magnet is used to study the magnetic recovery of the

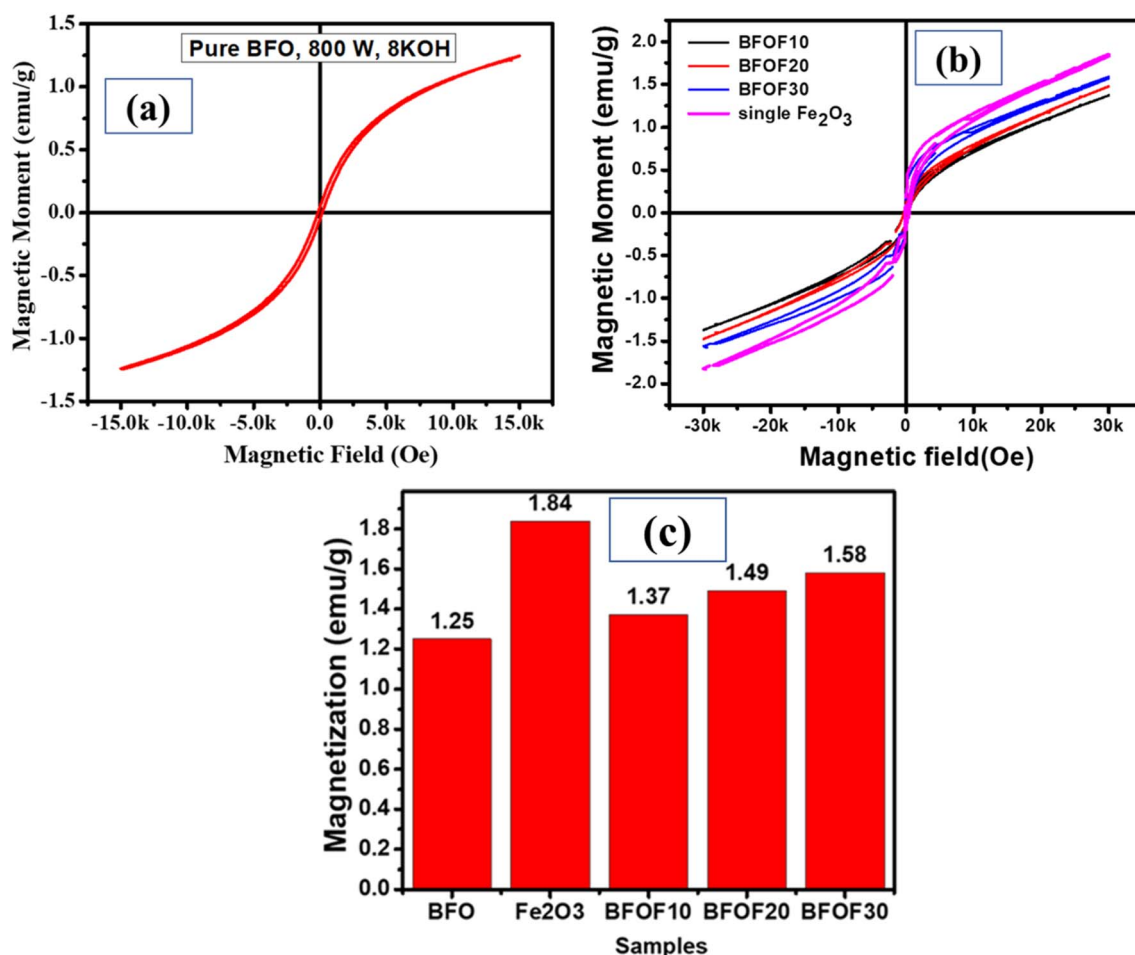


Fig. 8 Magnetic properties of (a) pure BFO, (b)  $Fe_2O_3$ , and the BFO- $Fe_2O_3$  composite and (c) magnetization values of pure phase BFO,  $Fe_2O_3$ , and the BFO- $Fe_2O_3$  composite.



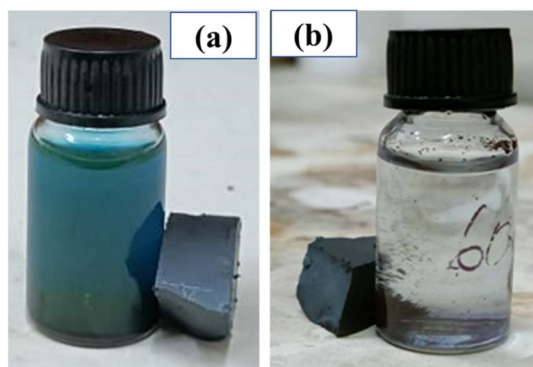


Fig. 9 Methylene blue solution post-photocatalytic test for pure (a) BFO and (b) BFOF30 and their magnetic recovery.

BFO and BFOF30 catalysts from the MB solution by applying a 1.5 T magnetic field for 6 minutes. Fig. 9(a) highlights how pure-phase BFO magnetic responses fail to recover particles when magnetic fields are applied after the photodegradation experiment. Therefore, additional filtering or centrifugation is required to separate the pure-phase BFO catalyst from the MB solution.

To study the magnetic recovery of the most effective photocatalyst, BFOF30, we have applied the magnetic field, as shown in Fig. 9(b). Fig. 9(b) shows that BFOF30 could be recovered when applying a magnetic field, confirming its excellent magnetic recovery. It is essential to highlight that the BFOF30 magnetic response is strong for recovering particles by applying magnetic fields, indicating no further filtering or centrifugation methods are required. The results of these stability and recovery studies indicate that the stability and magnetic recovery properties of BFO improved when hollow spherical  $\text{Fe}_2\text{O}_3$  was added to BFO.

At the beginning and end of the photocatalytic process and recovery test for BFOF30, XRD was used on the BFOF30 powder

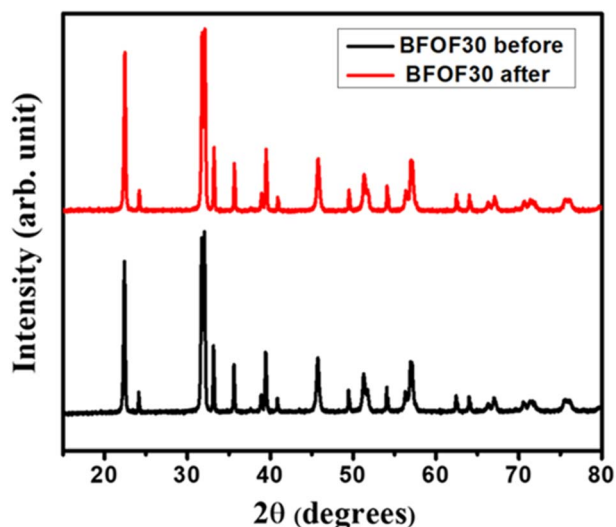


Fig. 10 XRD patterns of the BFOF30 composite pre and post photocatalytic tests for BFOF30.

to determine if it could be recovered. Fig. 10 shows the XRD patterns of BFOF30 pre- and post-degradation of MB. For the BFOF30 catalyst used in the photocatalysis experiment, we found no variations in the XRD patterns or traces from MB. Therefore, magnetically recovered BFOF30 catalysts maintain their original structural features, improving their reuse potential.

## 5.8. Conclusion

In summary,  $\text{BiFeO}_3\text{-Fe}_2\text{O}_3$  composites were successfully synthesized by a microwave-assisted co-precipitation method for MB degradation. UV-vis absorption spectroscopy and microstructural analysis demonstrate that micro interfaces between BFO and  $\text{Fe}_2\text{O}_3$  microspheres can alter band gaps and change work functions at their surface. Due to this, it is simpler to form electron-hole pairs and more difficult for them to recombine. In the best results, BFOF30 showed 94% degradation of MB after 70 minutes of exposure to sunlight. According to the magnetic study, BFOF10, BFOF20, and BFOF30 phases have the highest magnetization values compared to pure phase BFO. A stability and recovery test showed that the photocatalyst BFOF30 could be recovered and reused at least four times with an average efficiency reduction of 4%. Therefore, the  $\text{BFO-Fe}_2\text{O}_3$  composites display enhanced photocatalytic efficiency when a direct Fenton-like mechanism and an electron drain process coexist.

## Conflicts of interest

There are no conflicts to declare.

## Acknowledgements

Pravallika Banoth acknowledges the National Fellowship for Scheduled Tribe Students (NFST) for SRF, funded by the Ministry of Tribal Affairs, Government of India (No. 19012/03/2018-Sch). We acknowledge the facilities provided by the University Grants Commission-Networking Resources (UGC-NRC) of the School of Physics, University of Hyderabad, India. The authors acknowledge funding from the Institute of Eminence project, MHRD, UoH-IoE-RC2-21-017.

## References

- 1 C. Minero and D. Vione, A quantitative evaluation of the photocatalytic performance of  $\text{TiO}_2$  slurries, *Appl. Catal. B*, 2006, **67**(3-4), 257-269.
- 2 H. Liu, X. Ren and L. Chen, Synthesis and characterization of magnetic metal-organic framework for the adsorptive removal of Rhodamine B from aqueous solution, *J. Ind. Eng. Chem.*, 2016, **34**, 278-285.
- 3 T. A. Gadhi, S. Hernández, M. Castellino, A. Chiodoni, T. Husak, G. Barrera, P. Allia, N. Russo and A. Tagliaferro, Single  $\text{BiFeO}_3$  and mixed  $\text{BiFeO}_3/\text{Fe}_2\text{O}_3/\text{Bi}_2\text{Fe}_4\text{O}_9$  ferromagnetic photocatalysts for solar light driven water

- oxidation and dye pollutants degradation, *J. Ind. Eng. Chem.*, 2018, **63**, 437–448.
- 4 Y. Fu and X. Wang, Magnetically separable  $\text{ZnFe}_2\text{O}_4$ -graphene catalyst and its high photocatalytic performance under visible light irradiation, *Ind. Eng. Chem. Res.*, 2011, **50**(12), 7210–7218.
- 5 T. A. Gad-Allah, S. Kato, S. Satokawa and T. Kojima, Treatment of synthetic dyes wastewater utilizing a magnetically separable photocatalyst ( $\text{TiO}_2/\text{SiO}_2/\text{Fe}_3\text{O}_4$ ): parametric and kinetic studies, *Desalination*, 2009, **244**(1–3), 1–11.
- 6 S. Xuan, W. Jiang, X. Gong, Y. Hu and Z. Chen, Magnetically separable  $\text{Fe}_3\text{O}_4/\text{TiO}_2$  hollow spheres: fabrication and photocatalytic activity, *J. Phys. Chem. C*, 2009, **113**(2), 553–558.
- 7 F. Zheng, M. Shen, R. Guo, L. Fang and W. Dong, Magnetically separable  $\text{BiFeO}_3$  nanoparticles with a  $g\text{-Fe}_2\text{O}_3$  parasitic phase: controlled fabrication and enhanced visible-light photocatalytic activity, *J. Mater. Chem.*, 2011, **21**, 18645–18652.
- 8 Y. Liu, L. Yu, Y. Hu, C. Guo, F. Zhang and X. W. D. Lou, A magnetically separable photocatalyst based on nest-like  $\gamma\text{-Fe}_2\text{O}_3/\text{ZnO}$  double-shelled hollow structures with enhanced photocatalytic activity, *Nanoscale*, 2012, **4**(1), 183–187.
- 9 M. He, D. Li, D. Jiang and M. Chen, Magnetically separable  $\gamma\text{-Fe}_2\text{O}_3@ \text{SiO}_2@ \text{Ce-doped TiO}_2$  core-shell nanocomposites: Fabrication and visible-light-driven photocatalytic activity, *J. Solid State Chem.*, 2012, **192**, 139–143.
- 10 Z. Lou, F. Li, J. Deng, L. Wang and T. Zhang, Branch-like hierarchical heterostructure ( $\alpha\text{-Fe}_2\text{O}_3/\text{TiO}_2$ ): a novel sensing material for trimethylamine gas sensor, *ACS Appl. Mater. Interfaces*, 2013, **5**(23), 12310–12316.
- 11 Q. Chen, J. Li, X. Li, K. Huang, B. Zhou, W. Cai and W. Shangguan, Visible-light responsive photocatalytic fuel cell based on  $\text{WO}_3/\text{W}$  photoanode and  $\text{Cu}_2\text{O}/\text{Cu}$  photocathode for simultaneous wastewater treatment and electricity generation, *Environ. Sci. Technol.*, 2012, **46**(20), 11451–11458.
- 12 M. Mishra and D. M. Chun,  $\alpha\text{-Fe}_2\text{O}_3$  as a photocatalytic material: A review, *Appl. Catal., A*, 2015, **498**, 126–141.
- 13 C. M. Suarez, S. Hernández and N. Russo,  $\text{BiVO}_4$  as photocatalyst for solar fuels production through water splitting: a short review, *Appl. Catal., A*, 2015, **504**, 158–170.
- 14 K. R. Tolod, S. Hernández and N. Russo, Recent advances in the  $\text{BiVO}_4$  photocatalyst for sun-driven water oxidation: top-performing photoanodes and scale-up challenges, *Catalysts*, 2017, **7**(1), 13.
- 15 L. Chen, R. Huang, M. Xiong, Q. Yuan, J. He, J. Jia, M. Y. Yao, S. L. Luo, C. T. Au and S. F. Yin, Room-Temperature Synthesis of Flower-Like  $\text{BiOX}$  ( $\text{X} = \text{Cl}, \text{Br}, \text{I}$ ) Hierarchical Structures and Their Visible-Light Photocatalytic Activity, *Inorg. Chem.*, 2013, **52**(19), 11118–11125.
- 16 K. Natarajan, H. C. Bajaj and R. J. Tayade, Photocatalytic efficiency of bismuth oxyhalide ( $\text{Br}, \text{Cl}$  and  $\text{I}$ ) nanoplates for RhB dye degradation under LED irradiation, *J. Ind. Eng. Chem.*, 2016, **34**, 146–156.
- 17 S. Lee, Y. Park, D. Pradhan and Y. Sohn,  $\text{AgX}$  ( $\text{X} = \text{Cl}, \text{Br}, \text{I}$ )/ $\text{BiOX}$  nanoplates and microspheres for pure and mixed (methyl orange, rhodamine B and methylene blue) dyes, *J. Ind. Eng. Chem.*, 2016, **35**, 231–252.
- 18 Y. Yan, Z. Zhou, Y. Cheng, L. Qiu, C. Gao and J. Zhou, Template-free fabrication of  $\alpha$ - and  $\beta\text{-Bi}_2\text{O}_3$  hollow spheres and their visible light photocatalytic activity for water purification, *J. Alloys Compd.*, 2014, **605**, 102–108.
- 19 X. Xiao, R. Hu, C. Liu, C. Xing, C. Qian, X. Zuo, J. Nan and L. Wang, Facile large-scale synthesis of  $\beta\text{-Bi}_2\text{O}_3$  nanospheres as a highly efficient photocatalyst for the degradation of acetaminophen under visible light irradiation, *Appl. Catal. B*, 2013, **140**, 433–443.
- 20 M. Schlesinger, M. Weber, S. Schulze, M. Hietschold and M. Mehring, Metastable  $\beta\text{-Bi}_2\text{O}_3$  Nanoparticles with Potential for Photo-catalytic Water Purification Using Visible Light Irradiation, *ChemistryOpen*, 2013, **2**, 146–155.
- 21 F. Zheng, M. Shen, R. Guo, L. Fang and W. Dong, Magnetically separable  $\text{BiFeO}_3$  nanoparticles with a  $g\text{-Fe}_2\text{O}_3$  parasitic phase: controlled fabrication and enhanced visible-light photocatalytic activity, *J. Mater. Chem.*, 2011, **21**, 18645–18652.
- 22 S. M. Selbach, T. Tybell, M. A. Einarsrud and T. Grande, Size-dependent properties of multiferroic  $\text{BiFeO}_3$  nanoparticles, *Chem. Mater.*, 2007, **19**(26), 6478–6484.
- 23 D. Chen, Z. Wang, T. Ren, H. Ding, W. Yao, R. Zong and Y. Zhu, Influence of defects on the photocatalytic activity of  $\text{ZnO}$ , *J. Phys. Chem. C*, 2014, **118**(28), 15300–15307.
- 24 M. Mishra and D. M. Chun,  $\alpha\text{-Fe}_2\text{O}_3$  as a photocatalytic material: A review, *Appl. Catal., A*, 2015, **498**, 126–141.
- 25 H. Wang, L. Zhang, Z. Chen, J. Hu, S. Li, Z. Wang, J. Liu and X. Wang, Semiconductor heterojunction photocatalysts: design, construction, and photocatalytic performances, *Chem. Soc. Rev.*, 2014, **43**(15), 5234–5244.
- 26 S. Li, Y. H. Lin, B. P. Zhang, J. F. Li and C. W. Nan,  $\text{BiFeO}_3/\text{TiO}_2$  core-shell structured nanocomposites as visible-active photocatalysts and their optical response mechanism, *J. Appl. Phys.*, 2009, **105**(5), 054310.
- 27 F. Niu, D. Chen, L. Qin, N. Zhang, J. Wang, Z. Chen and Y. Huang, Facile synthesis of highly efficient p-n heterojunction  $\text{CuO}/\text{BiFeO}_3$  composite photocatalysts with enhanced visible-light photocatalytic activity, *ChemCatChem*, 2015, **7**(20), 3279–3289.
- 28 T. Fan, C. Chen, Z. Tang, Y. Ni and C. Lu, Synthesis and characterization of  $g\text{-C}_3\text{N}_4/\text{BiFeO}_3$  composites with an enhanced visible light photocatalytic activity, *Mater. Sci. Semicond. Process.*, 2015, **40**, 439–445.
- 29 Y. Cui, J. Briscoe, Y. Wang, N. V. Tarakina and S. Dunn, Enhanced photocatalytic activity of heterostructured ferroelectric  $\text{BaTiO}_3/\alpha\text{-Fe}_2\text{O}_3$  and the significance of interface morphology control, *ACS Appl. Mater. Interfaces*, 2017, **9**(29), 24518–24526.
- 30 X. Zheng, M. Huang, Y. You, H. Peng and J. Wen, Core-shell structured  $\alpha\text{-Fe}_2\text{O}_3@ \text{CeO}_2$  heterojunction for the enhanced visible-light photocatalytic activity, *Mater. Res. Bull.*, 2018, **101**, 20–28.

- 31 M. M. Can, T. Firat and Ş. Özcan, Interparticle interaction effects on magnetic behaviors of hematite ( $\alpha$ -Fe<sub>2</sub>O<sub>3</sub>) nanoparticles, *Physica B Condens.*, 2011, **406**(13), 2483–2487.
- 32 C. H. Yang, D. Kan, I. Takeuchi, V. Nagarajan and J. Seidel, Doping BiFeO<sub>3</sub>: approaches and enhanced functionality, *Phys. Chem. Chem. Phys.*, 2012, **14**(46), 15953–15962.
- 33 S. Y. Yang, L. W. Martin, S. J. Byrnes, T. E. Conry, S. R. Basu, D. Paran, L. Reichertz, J. Ihlefeld, C. Adamo, A. Melville and Y. H. Chu, Photovoltaic effects in BiFeO<sub>3</sub>, *Appl. Phys. Lett.*, 2009, **95**(6), 062909.
- 34 D. K. Mishra and X. Qi, Energy levels and photoluminescence properties of nickel-doped bismuth ferrite, *J. Alloys Compd.*, 2010, **504**(1), 27–31.
- 35 A. Zhu, Q. Zhao, X. Li and Y. Shi, BiFeO<sub>3</sub>/TiO<sub>2</sub> nanotube arrays composite electrode: construction, characterization, and enhanced photoelectrochemical properties, *ACS Appl. Mater. Interfaces*, 2014, **6**(1), 671–679.
- 36 J. Wu, Z. Fan, D. Xiao, J. Zhu and J. Wang, Multiferroic bismuth ferrite-based materials for multifunctional applications: ceramic bulks, thin films and nanostructures, *Prog. Mater. Sci.*, 2016, **84**, 335–402.
- 37 S. H. Lim, M. Murakami, J. H. Yang, S. Y. Young, J. Hatrick-Simpers, M. Wuttig, L. G. Salamanca-Riba and I. Takeuchi, Enhanced dielectric properties in single crystal-like BiFeO<sub>3</sub> thin films grown by flux-mediated epitaxy, *Appl. Phys. Lett.*, 2008, **92**(1), 012918.
- 38 M. Arredondo, Q. M. Ramasse, K. Bogle and V. Nagarajan, Chemistry of the Fe<sub>2</sub>O<sub>3</sub>/BiFeO<sub>3</sub> interface in BiFeO<sub>3</sub> thin film heterostructures, *Materials*, 2010, **3**(12), 5274–5282.
- 39 T. A. Gadhi, S. Hernández, M. Castellino, A. Chiodoni, T. Husak, G. Barrera, P. Allia, N. Russo and A. Tagliaferro, Single BiFeO<sub>3</sub> and mixed BiFeO<sub>3</sub>/Fe<sub>2</sub>O<sub>3</sub>/Bi<sub>2</sub>Fe<sub>4</sub>O<sub>9</sub> ferromagnetic photocatalysts for solar light driven water oxidation and dye pollutants degradation, *J. Ind. Eng. Chem.*, 2018, **63**, 437–448.
- 40 F. Zheng, M. Shen, R. Guo, L. Fang and W. Dong, Magnetically separable BiFeO<sub>3</sub> nanoparticles with a g-Fe<sub>2</sub>O<sub>3</sub> parasitic phase: controlled fabrication and enhanced visible-light photocatalytic activity, *J. Mater. Chem.*, 2011, **21**, 18645–18652.
- 41 T. A. Gadhi, S. Hernández, M. Castellino, A. Chiodoni, T. Husak, G. Barrera, P. Allia, N. Russo and A. Tagliaferro, Single BiFeO<sub>3</sub> and mixed BiFeO<sub>3</sub>/Fe<sub>2</sub>O<sub>3</sub>/Bi<sub>2</sub>Fe<sub>4</sub>O<sub>9</sub> ferromagnetic photocatalysts for solar light driven water oxidation and dye pollutants degradation, *J. Ind. Eng. Chem.*, 2018, **63**, 437–448.
- 42 R. Zhang, S. Liu, F. Kong, J. Tong, L. Ruan, Q. Duan, J. Zhou and X. Zhang,  $\alpha$ -Fe<sub>2</sub>O<sub>3</sub>/BiFeO<sub>3</sub> composites as visible-active photocatalysts and their optical response mechanism, *J. Phys. Chem. Solids*, 2020, **141**, 109329.
- 43 P. Banoth, A. Sohan, C. Kandula, R. K. Kanaka and P. Kollu, Microwave-Assisted Solvothermal Route for One-Step Synthesis of Pure Phase Bismuth Ferrite Microflowers with Improved Magnetic and Dielectric Properties, *ACS Omega*, 2022, **7**(15), 12910–12921.
- 44 L. De Los Santos Valladares, L. L. Félix, S. E. Suarez, A. B. Dominguez, T. Mitrelias, S. Holmes, N. O. Moreno, J. A. Aguiar and C. H. W. Barnes, Preparation and crystallization of hollow  $\alpha$ -Fe<sub>2</sub>O<sub>3</sub> microspheres following the gas-bubble template method, *Mater. Chem. Phys.*, 2016, **169**, 21–27.
- 45 J. Kargin, L. Valladares, L. E. Borja-Castro, J. Xize, D. G. Mukhambetov, Y. V. Konyukhov, N. O. Moreno, A. G. Dominguez and C. H. W. Barnes, Characterization of iron oxide waste scales obtained by rolling mill steel industry, *Hyperfine Interact.*, 2022, **243**(1), 1–11.
- 46 P. Banoth, A. Sohan, C. Kandula, R. K. Kanaka and P. Kollu, Microwave-Assisted Solvothermal Route for One-Step Synthesis of Pure Phase Bismuth Ferrite Microflowers with Improved Magnetic and Dielectric Properties, *ACS Omega*, 2022, **7**(15), 12910–12921.
- 47 B. Sun, P. Han, W. Zhao, Y. Liu and P. Chen, White-light-controlled magnetic and ferroelectric properties in multiferroic BiFeO<sub>3</sub> square nanosheets, *J. Phys. Chem. C*, 2014, **118**(32), 18814–18819.
- 48 R. C. Haislmaier, N. J. Podraza, S. Denev, A. Melville, D. G. Schlom and V. Gopalan, Large nonlinear optical coefficients in pseudo-tetragonal BiFeO<sub>3</sub> thin films, *Appl. Phys. Lett.*, 2013, **103**(3), 031906.
- 49 Q. I. Rahman, M. Ahmad, S. K. Misra and M. Lohani, Effective photocatalytic degradation of rhodamine B dye by ZnO nanoparticles, *Mater. Lett.*, 2013, **91**, 170–174.
- 50 M. Tayebi, A. Tayebi, T. Soltani and B. K. Lee, pH-Dependent photocatalytic performance of modified bismuth vanadate by bismuth ferrite, *New J. Chem.*, 2019, **43**(23), 9106–9115.
- 51 T. K. Dixit, S. Sharma and A. S. K. Sinha, Synergistic effect of N-rGO supported Gd doped bismuth ferrite heterojunction on enhanced photocatalytic degradation of rhodamine B, *Mater. Sci. Semicond. Process.*, 2021, **123**, 105538.
- 52 F. Niu, D. Chen, L. Qin, N. Zhang, J. Wang, Z. Chen and Y. Huang, Facile synthesis of highly efficient p-n heterojunction CuO/BiFeO<sub>3</sub> composite photocatalysts with enhanced visible-light photocatalytic activity, *ChemCatChem*, 2015, **7**(20), 3279–3289.
- 53 L. De Los Santos Valladares, A. Bustamante Dominguez, L. León Félix, J. B. Kargin, D. G. Mukhambetov, A. L. Kozlovskiy, N. O. Moreno, J. Flores Santibañez, R. Castellanos Cabrera and C. H. W. Barnes, Characterization and magnetic properties of hollow  $\alpha$ -Fe<sub>2</sub>O<sub>3</sub> microspheres obtained by sol gel and spray roasting methods, *J. Sci.: Adv. Mater. Devices*, 2019, **4**, 483–491.